www.czasopisma.pan.pl www.journals.pan.pl
Chemical and Process Engineering 2020, 41 (1), 25–44
DOI: 10.24425/cpe.2019.130221

TYRE-DERIVED ACTIVATED CARBON – TEXTURAL PROPERTIES AND MODELLING OF ADSORPTION EQUILIBRIUM OF *n*-HEXANE

Tomasz Kotkowski, Robert Cherbański*, Eugeniusz Molga

Warsaw University of Technology, Faculty of Chemical and Process Engineering,
ul. Waryńskiego 1, Warsaw, Poland

There is general agreement that primary pyrolysis products of end-of-life tyres should be valorised to improve the economics of pyrolysis. In this work, tyre pyrolysis char (TPC) is produced in a pyrolysis pilot plant designed and built at our home university. The produced TPC was upgraded to tyre-derived activated carbon (TDAC) by activation with CO_2, and then characterised using stereological analysis (SA) and nitrogen adsorption at 77 K. SA showed that the grains of TPC and TDAC were quasi-spherical and slightly elongated with a 25% increase in the mean particle cross-section surface area for TDAC. The textural properties of TDAC demonstrated the BET and micropore surface areas of 259 and 70 m^2/g, respectively. Micropore volume and micropore surface area were 5.8 and 6.7 times higher for TDAC than TPC at $\sim$ 2 nm, respectively. The *n*-hexane adsorption was investigated using experiments and modelling. Eight adsorption isotherms along with three error functions were tested to model the adsorption equilibrium. The optimum sets of isotherm parameters were chosen by comparing sum of the normalized errors. The analysis indicated that the Freundlich isotherm gave the best agreement with the equilibrium experiments. In relation to different activated carbons, the adsorption capacity of TDAC for *n*-hexane is about 16.2 times higher than that of the worst reference material and 4.3 times lower than that of the best reference material. In addition, stereological analysis showed that activation with CO_2 did not change the grain's shape factors. However, a 25% increase in the mean particle cross-section surface area for TDAC was observed.

Keywords: adsorption, *n*-hexane, tyre-derived activated carbon, pyrolysis, tyres

1. INTRODUCTION

There are two types of used tyres: part-worn tyres and end-of-life tyres (ELTs). Part-worn tyres are reusable as a purchase on the second-hand market or after re-treading. On the other hand, ELTs cannot be reused on vehicles anymore. According to World Business Council for Sustainable Development, one billion ELTs are generated globally each year (WBCSD, 2008). In the EU28, the total mass of generated ELTs increased from 2.73 to 2.95 million tonnes in the period 2014–2016 (ETRMA, 2018; 2017). Although ELTs are classified as non-hazardous waste (Council Directive 91/156/EEC), direct disposal of ELTs in landfills is banned in the majority of developed countries. In the EU, this issue is regulated by Directive on the Landfill of Waste (Council Directive 1999/31/EC). According to this law, landfills of whole and shredded ELTs are prohibited.

Problems associated with landfilling and stockpiles of ELTs concern landfill fires with emissions of toxic gases, contamination of surface and groundwater and even health risks from mosquitoes which are possible

---

* Corresponding author, e-mail: Robert.Cherbanski@pw.edu.pl

in certain regions of the world (diseases such as West Nile fever, dengue fever and malaria). Tyres are flammable and tyre fire is very difficult to extinguish. When tyre fire occurs, air is polluted with toxic gases such as: polycyclic aromatic hydrocarbons, benzene, styrene, phenols and butadiene. Moreover, oil from melted tyres contaminates soil and water (WBCSD, 2008).

To reduce the negative impact of tyres on health and the environment, they must be processed in a sustainable manner. There are the following recovery routes of ELTs: material recovery and energy recovery (WBCSD, 2008).

Within the concept of material recovery, whole, shredded and ground ELTs are used in various civil engineering applications such as: coastal protection, slope stabilisation, road embankments, sound barriers, rubber-modified asphalt, running tracks, sports fields and flooring for playgrounds, to mention some of them.

Since ELTs have a caloric value equivalent to petroleum coke, which is even higher than coal, they are often used as supplementary fuel, mainly in cement kilns, but also in thermal power stations, pulp and paper mills, steel mills and industrial boilers. The tyre-derived fuel (TDF) as a low-cost source of energy is especially popular in Japan where 70% of ELTs are used in cement kilns, paper mills and tire factories (WBCSD, 2008). To a lesser extent TDF is used in the US (53% of ELTs) and the UE (41% of ELTs). Pyrolysis is one of the increasingly common ELT processing technologies. The process consists in the thermal decomposition of ELTs in the absence of air. The primary pyrolysis products are char (33%), oil (35%) and gas (20%) and metal (12%) (Sharma et al., 1998).

In general, the surface area of the pyrolysis char is less than 100 m^2g^{-1} (Antoniou et al., 2014; Mui et al., 2004). Surface areas between 65 and 84 m^2g^{-1} were reported for the char produced in a fixed bed reactor (Williams, 2013). Similar values were obtained for chars produced in a rotary kiln reactor, ~ 89 m^2g^{-1} (Li et al., 2004) and in a fluidised bed reactor, 76–85 m^2g^{-1}, in the temperature range of 773–873 K (Kaminsky and Mennerich, 2001). To develop the surface area of char and to improve its adsorptive properties, activation is required. In the majority studies, activation is performed with CO_2 or steam. The reported BET surface areas are within wide ranges: between 250 and 1014 m^2/g for CO_2 activation, and between 272 and 1317 m^2/g for steam activation (Antoniou et al., 2014).

Activated carbons obtained from TPCs have been successfully applied for purification of water from: different dyes (Acevedo et al., 2015; Daraei and Mittal, 2017; Shaid et al., 2019; Song et al., 2014), phenol (Helleur et al., 2001; Li et al., 2005; San Miguel et al., 2002; San Miguel et al., 2003), Bisphenol A (Acosta et al., 2018), other organic compounds such as: 1,3-dichlorbenzene, 1,3-dinitrobenzene, 2,4-dichlorophenol (Lian et al., 2011), 2-chlorophenol (Manirajah et al., 2019), toluene (Zhu et al., 2011), metals ions: Co(II), Cr(VI), Cu(II), Ni(II), Pb(II) (Abbasi et al., 2019; Makrigianni et al., 2017; Saleh et al., 2013), and rare earth elements (Smith et al., 2016).

On the other hand, there are few studies on gas phase adsorption of TDACs. Previous works concern adsorption of polycyclic aromatic hydrocarbons (Aranda et al., 2007; Murillo et al., 2005), nitrogen dioxide (Hofman and Pietrzak, 2011), mercury chloride (Lehmann et al., 1998; Lin et al., 2006), trace metals such as mercury (Charpenteau et al., 2007; Lehmann et al., 1998) and arsenic (Charpenteau et al., 2007), and 2,3,7,8-substituted PCDD/F (Hajizadeh et al., 2011). Only a few studies have been carried out on VOC adsorption (Allen et al., 1999; Lehmann et al., 1998).

Indeed, the emission of VOCs is a serious global environmental problem. The problem is regulated in the European Union by the Paints Directive (Directive 2004/42/CE) and the Industrial Emissions Directive (Directive 2010/75/EU). *n*-hexane, being a model VOC in this work, is an aliphatic saturated hydrocarbon obtained from petroleum with a boiling point at about 341 K. *n*-hexane is used in the formulation of glues for shoes, leather products and roofing. It is also widely used as a solvent for exacting oils from seeds, for cleansing, degreasing and in textile manufacturing. The emission of *n*-hexane causes air pollution and significant damage to human health including occupational neuropathies.

In general, VOCs can be recovered using several techniques such as: absorption, adsorption, condensation and membrane separation. Basically, adsorption covers the range of VOC concentration from 20 ppm to about one-fourth of the Lower Explosive Limit (LEL). Nevertheless, adsorption is economically viable rather at the lower limit of this range. On the other hand, incinerators, membranes, and condensers are better choice when VOC concentrations are at the other limit of this range (E.P.A. Clean Air Technology, 1999).

The tested porous materials have been characterised by stereological analysis and nitrogen adsorption at 77 K. Stereological analysis (SA) provides complementary information to data obtained from the analysis of nitrogen isotherms. While a nitrogen isotherm (at 77 K) provides data on the texture of a porous material (e.g. BET surface area, pore geometry, pore size distribution), SA enables to calculate e.g.: external surface area of particles, equivalent grain diameter, sphericity of grains, mean perimeter of two-dimensional cross sections of materials. In general, SA enables reconstruction of the 3D structure of an object based on its 2D image. Most frequently, modern electron microscopy in scanning or transmission mode is used to obtain 2D images of the samples.

SA was previously employed to show changes occurring during processing of nano-metals by different methods (Wejrzanowski and Kurzydlowski, 2003) and to optimise the microstructures of nano-polycrystalline materials and nano-composites (Wejrzanowski et al., 2010). SA was also successfully applied for the assessment of service degradation of materials in petrochemical installation (Wejrzanowski et al., 2008). In recent years, SA has been used to characterise the microstructure of mullite foam with hierarchical microstructure (Gregorová et al., 2018) and transparent Yttrium-aluminum garnet ceramics (Uhlířová et al., 2014).

Our knowledge of VOC adsorption on TDACs is based on very limited data. Thus, the aim of this work was to characterise this new material by nitrogen adsorption at 77 K and SA and to test several adsorption isotherm models describing adsorption equilibrium of *n*-hexane on TDAC.

2. EXPERIMENTAL

2.1. Materials

Nitrogen 6.0 (Messer, Poland), and helium 5.0 (Multax, Poland) were used to perform analyses in a surface characterisation analyser. For vapour analysis, *n*-hexane (CAS 110-54-3; purity ≥ 99%), purchased from Chempur (Poland), was used. A separate nitrogen gas cylinder 5.0 (Multax, Poland) was used with a degasser unit. Nitrogen 5.0 and carbon dioxide 4.5 (Multax, Poland) were used for activation of TPC in an electric tube furnace. TPC was produced in a pyrolysis pilot plant (see section 2.2).

2.2. Methods

The pyrolysis pilot plant was designed and built at our home university within a project aimed at the development of a method for continuous large scale pyrolysis of ELTs (Fig. 1). The pyrolysis pilot plant comprised a batch tank reactor equipped with a low-speed scraping stirrer (approx. 10 rpm), a two-section condenser, a pyrolysis oil tank, being also a gas-liquid separator, and a non-condensing pyrolysis gas burner. The diameter and length of the reactor chamber were 0.31 and 1.06 m, respectively. Its working volume was approx. 75 dm^3. The pyrolysis reactor was heated using a 7.4 kW electric heater.

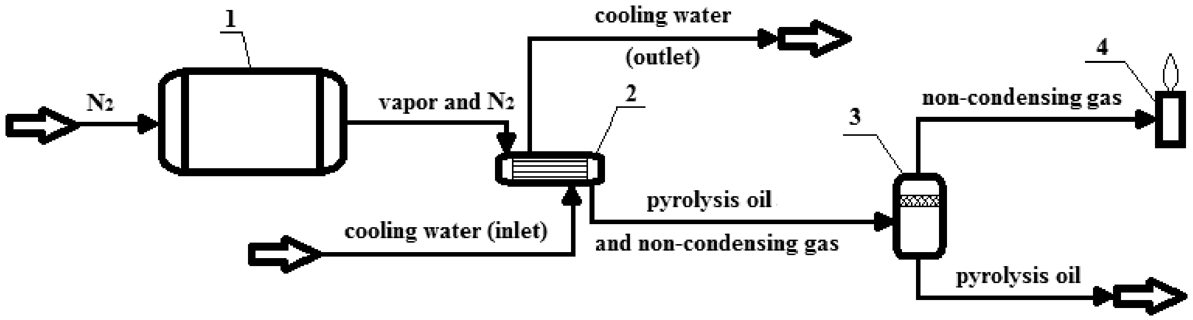

Fig. 1. Schematic diagram of the pyrolysis pilot plant from which TPC was obtained; 1 – pyrolysis reactor with a batch of shredded ELTs, 2 – two-section condenser, 3 – oil tank (gas-liquid separator), 4 – gas burner

TPC was produced from shredded ELTs of different types and brands, which were pre-treated to remove steel cords. About 20 kg of ELTs were pyrolysed at 773 K under nitrogen atmosphere. The following approximate yields of char, oil and gas were obtained in this measurement: 39%, 55% and 6% by mass, respectively.

Activation of the pyrolysis char was performed in an electric tube furnace. The activation was carried out under CO_2 atmosphere for 135 min with a flow rate of 0.5 dm^3/min at 1373 K. The TPC samples were heated/cooled before/after the activation step by nitrogen with a flow rate of 0.5 dm^3/min. The activation temperature and its approximate duration were determined on the basis of thermogravimetric analysis (TGA) reported in our previous work (Kotkowski et al., 2018). Unlike TGA, in which heat transfer resistance can be usually neglected, the temperature in the electric furnace was measured outside the ceramic tube with the sample, which posed a significant thermal resistance. Therefore, several CO_2-activated tyre pyrolysis chars were produced with increasing activation times. The sample with the highest BET surface area due to activation (259 m^2/g) was chosen to perform further equilibrium and stereological studies.

Outgassing of the samples was performed in the Smart VacPrep degasser (Micromeritics, USA). Samples of about 100 mg were outgassed under vacuum (about 1 Pa) using a two-stage temperature program: (1) 363 K for 1 h, and (2) 573 K for 24 h. Outgassing removed adsorbed gases and vapours from the samples.

The 3Flex Surface Characterization Analyser (Micromeritics, USA) was used to examine the surface characteristics of the samples. All calculations were performed using the nitrogen adsorption isotherms at 77 K. The BET surface area was calculated from a BET plot in the appropriate pressure range determined according to the procedure proposed by Rouquerol (Rouquerol et al., 2007). Thus, the relative pressure ranges, which were found in this way, were 0.05–0.2 for TPC and 0.05–0.16 for TDAC. Porosity distribution was calculated using Non-Local-Density-Functional Theory (NLDFT). The N2-NLDFT model was employed in the calculations assuming a slit-like pore geometry with the pore size range between 3.5 and 1000 Å (Tarazona, 1985a; 1985b; Tarazona et al., 1987).

A vapour source container (Micromeritics, USA) filled with *n*-hexane was used to carry out vapour adsorption on the outgassed sample. The vapour source temperature was set at 313 K and was controlled by a thermostated glass vessel with a jacket. Adsorption of *n*-hexane was performed for the temperature of 313 K.

The stereology-based image analysis was carried out using the MicroMeter software (Wejrzanowski et al., 2008). A few different techniques were employed to collect SEM images (taken by FEI Quanta 200 equipped with an EDAX detector), including: secondary electrons (SE), back-scattered electrons (BSE), a mixed mode of BSE and SE in a range of magnifications from 100 to 2000 times. A series of eight SEM images were taken for TPC and nine SEM images for TDAC.

Eight adsorption isotherms, namely: Langmuir, Freundlich, Sips, Toth, Extended Langmuir (EL), Aranovich–Donohue–Toth (A–D–Toth), Aranovich–Donohue–Sips (A–D–Sips) and Dubinin–Astakhov (D–A) were used to model *n*-hexane adsorption on TDAC. While the Langmuir isotherm refers to homogeneous adsorption, the other isotherms consider heterogeneous adsorption.

The Langmuir theory assumes localised adsorption occurring at specific active sites within the adsorbent (Langmuir, 1917; 1918). The theory assumes monolayer coverage of adsorbate over the adsorbent surface. Moreover, there are no interactions between adsorbed molecules on adjacent sites. The Langmuir isotherm can be written as follows.

$$q_e = q_{\max}\frac{K_L P}{1 + K_L P} \tag{1}$$

The Freundlich isotherm is an empirical equation which describes adsorption on heterogeneous surfaces (Freundlich, 1907). The Freundlich isotherm is given by the following equation.

$$q_e = K_F P^{1/n} \tag{2}$$

The Sips isotherm is a combination of the Langmuir and Freundlich isotherms (Sips, 1948). The Sips isotherm is given by the following equation.

$$q_e = q_m\frac{K_S P^{1/n}}{1 + K_S P^{1/n}} \tag{3}$$

The Toth isotherm is another form of an empirical equation developed to improve the fit of the Langmuir isotherm. The Toth isotherm is given by the following equation (Toth, 1971).

$$q_e = q_m\frac{K_T P}{[1 + (K_T P)^n]^{1/n}} \tag{4}$$

A general expression for a type II isotherm in the form of Eq. (5) was proposed by Aranovich and Donohue (1995).

$$q_e = \frac{f(P)}{(1 - P^0/P)^n} \tag{5}$$

Following this, the A–D–Toth (Eq. (6)) and A–D–Sips (Eq. (7)) isotherms were introduced to better describe the sigmoid shape of a type II isotherm (Zhang and Wang, 2010).

$$q_e = q_{\max}\frac{K_{\mathrm{ADT}} P}{\left[1 + (K_{\mathrm{ADT}} P)^t\right]^{1/t}(1 - P^0/P)^n} \tag{6}$$

$$q_e = q_{\max}\frac{(K_{\mathrm{ADS}} P)^{1/d}}{\left[1 + (K_{\mathrm{ADS}} P)^{1/d}\right](1 - P^0/P)^n} \tag{7}$$

The EL isotherm (Eq. (8)) was proposed to avoid a convergence problem during iterative calculations due to a singularity at pressure equal to saturation vapour pressure (Zhang and Wang, 2010).

$$q_e = q_{\max}\frac{K_{EL} P}{1 + K_{EL} P}e^{nP/P^0} \tag{8}$$

To account for the effect of temperature on adsorption equilibrium the following equation was introduced into Eqs. (1)–(4) and (6))–(8).

$$K_i = K_{i0}e^{\frac{-\Delta H_{ads}}{RT}} \tag{9}$$

The D–A isotherm (Eq. (10)) is a general form of the Dubinin–Radushkevich (D–R) equation introduced on the basis of the Theory of Volume Filling of Micropores (Dubinin et al., 1947).

$$Q_e = Q_0 e^{\left[-\left(\frac{\varepsilon}{\beta E_0}\right)^n\right]} \tag{10}$$

where ε is the adsorption potential, $\varepsilon = RT\ln\left(P^0/P\right)$.

The parameters of all used adsorption isotherms were calculated by nonlinear regression using Solver Add-in in Excel with the Generalized Reduced Gradient Nonlinear algorithm employed.

3. RESULTS AND DISCUSSION

Figure 2 shows a comparison of the nitrogen adsorption isotherms for TPC and TDAC. Goodness of fit of the N2-NLDFT model to the adsorption isotherms is also shown.

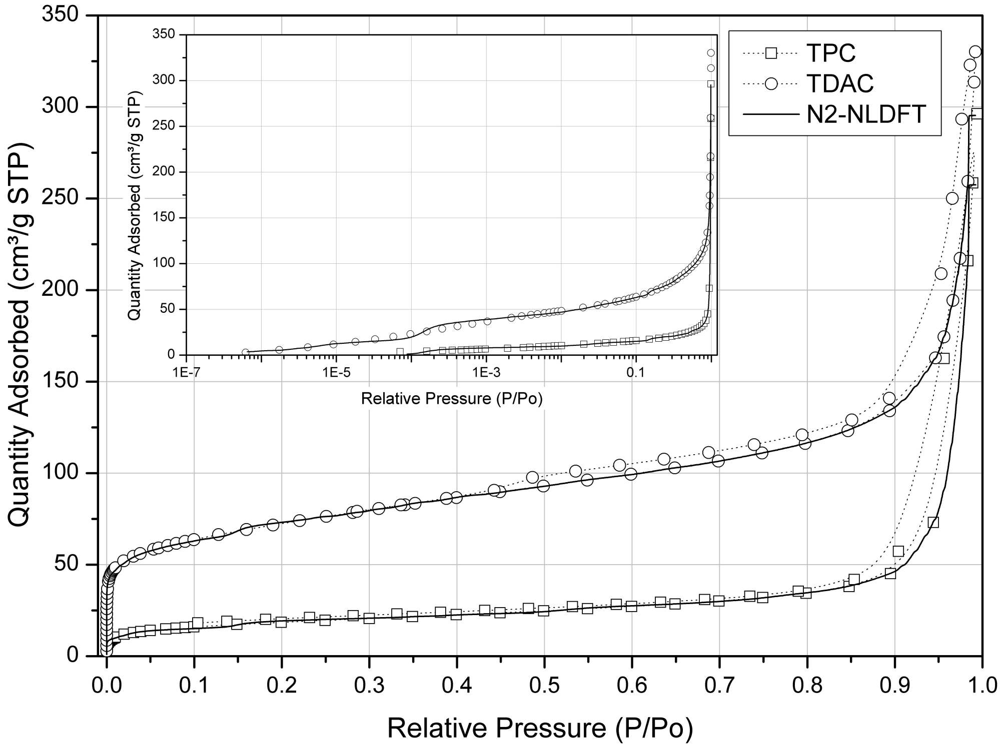

Fig. 2. Nitrogen adsorption/desorption isotherms for TPC and TDAC at 77 K (symbols with dotted lines). Goodness of fit of the N_2-NLDFT model to the experimental adsorption isotherms (solid lines). Standard deviations of fits: 7.59575 cm^3/g STP for TPC, 7.52704 cm^3/g STP for TDAC

According to the IUPAC recommendations released in 1985, physisorption isotherms were divided into six major types (Sing et al., 1985). Several years later, this primary classification was extended by introducing the subdivision of types I, II and IV (Rouquerol et al., 1998). Referring to this extended classification, the presented adsorption isotherms exhibit a type II(b) isotherm. Conversely to a type II(a) isotherm, which is reversible in the whole range of relative pressures, a type II(b) isotherm displays a type H3 hysteresis loop. That is, upon the initial reversible filling of micropores (< 2 nm), multilayer adsorption and capillary condensation take place in meso- (2–50 nm) and macropores (> 50 nm). Capillary condensation occurring in meso- and macropores can be seen as a hysteresis loop with a sharp increase of the adsorbed amount at pressures approaching the saturation pressure, i.e. $P/P^0 = 1$. Note that only the TDAC sample has the steep region of the desorption branch closing the hysteresis loops at ~ 0.42, which is typical for nitrogen hysteresis loops (Sing et al., 1985). On the other hand, the TPC sample exhibits low pressure hysteresis which can be connected to the change in volume of the adsorbent (i.e. the swelling of non-rigid pores) (Sing et al., 1985). The presence of the type H3 hysteresis loop is connected with slit-shaped pores. Given that a plateau is absent at high relative pressures for a type H3 hysteresis loop, the pore size distribution in the mesopore range cannot be precisely evaluated using classical methods based on the modified Kelvin equation, such as the Barrett–Joyner–Halenda (BJH) method. Instead, microscopic methods using statistical mechanics such as the NLDFT, Grand Canonical Monte Carlo or Molecular Dynamics can be successfully applied. Using these methods an accurate pore size analysis over the complete micro- and mesopore size range is possible.

Figures 3 and 4 show comparisons of pore size distributions (PSDs) and the cumulative pore volume and area for the TPC and TDAC samples. Results were calculated with the N2-NLDFT model over a large range of pore widths, i.e., from micropores up to the macropore range using the commercial MicroActive

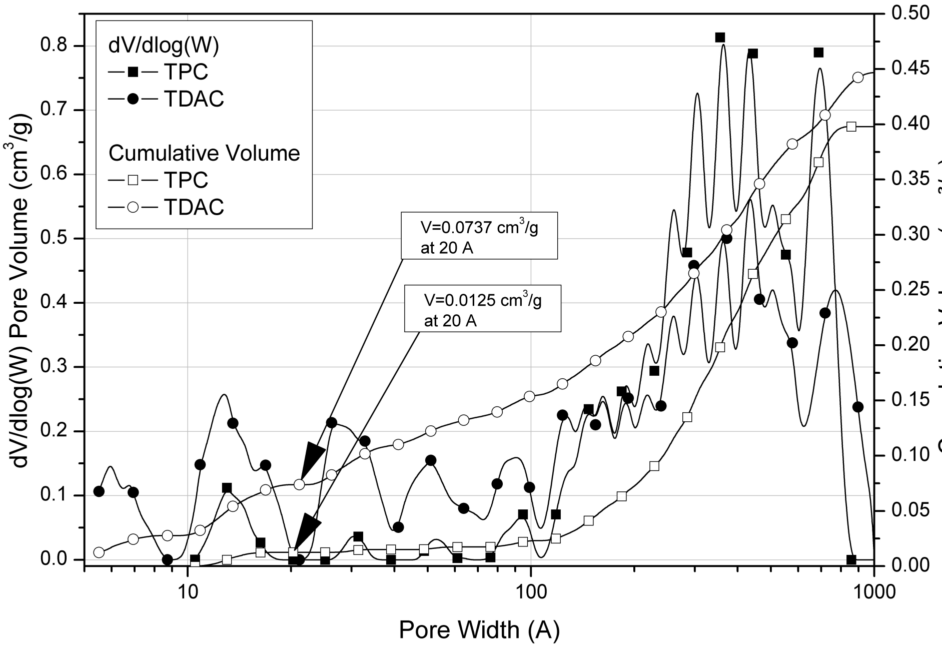

Fig. 3. Pore size distributions and cumulative pore volume for TPC and TDAC calculated with the N2-NLDFT model

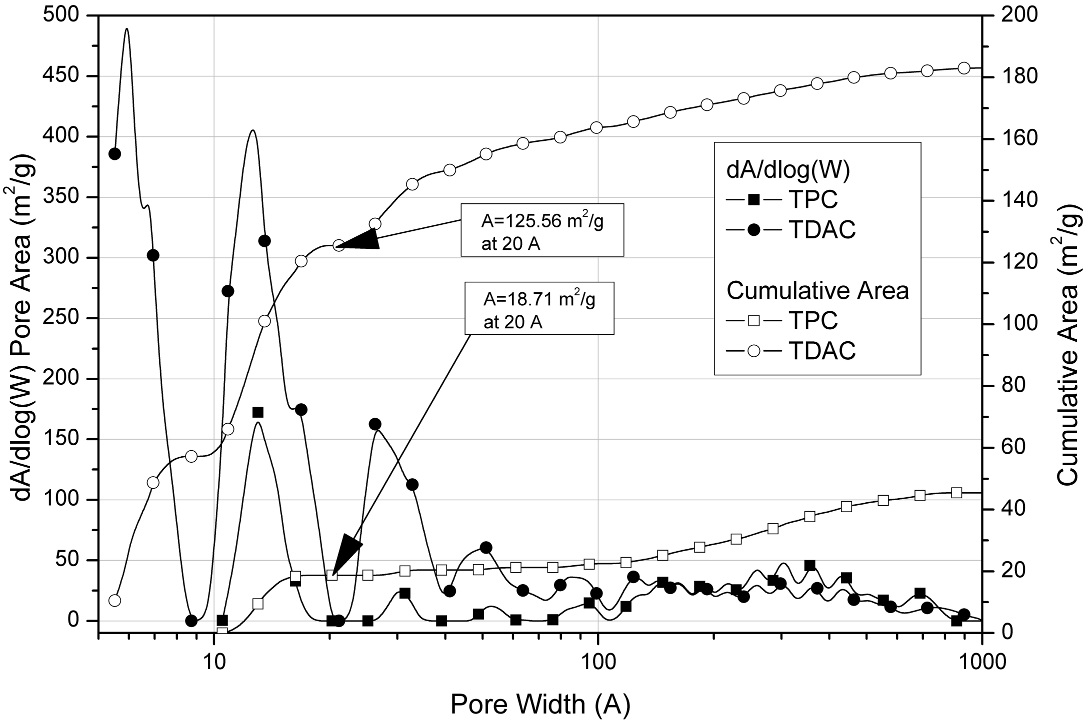

Fig. 4. Pore size distributions and cumulative pore area calculated with the N2–NLDFT model for TPC and TDAC

software (Micromeritics Instrument Corporation 2013-2014, 2014). Note that the model predictions are in almost complete agreement with the experimental data as shown in Fig. 2.

As VOC removal usually concerns diluted gas streams, which is connected with low relative pressures, microporous structure of an adsorbent is central for efficient VOC adsorption (Kosuge et al., 2007). In addition, n-hexane molecules are small enough (kinetic diameter is 0.43 nm, Cuadrado-Collados et al., 2019) to penetrate easily deep into the microporous structure. A careful comparison of PSDs presented in Figs. 3 and 4 shows that the microporous structure is better developed for TDAC than TPC. Note that this beneficial structure is maintained up to about 20 nm (200 Å), being within the mesopore size range. A comparison of the cumulative volume and cumulative surface area profiles for both samples shows that micropore volume and micropore surface area are about 5.8 and 6.7 times higher for TDAC than TPC at ~ 2 nm, respectively (Figs. 3 and 4).

Table 1 summarises data on porous structure of TDAC and TPC obtained from nitrogen adsorption at 77 K.

Table 1. Details on porous structure of TDAC and TPC

Sample name	TDAC	TPC
BET surface area [m^2/g]	259.1989 ± 0.4039	66.4748 ± 0.2817
BET C value	227	136
BET correlation coefficient	0.99999	0.99995
t-plot micropore surface area [m^2/g]	70.1113	13.0782
t-plot external surface area [m^2/g]	189.0876	53.3966
Total pore volume by the Gurvich method [cm^3/g]	0.511 at $P/P^0 = 0.992$	0.459 at $P/P^0 = 0.994$
BJH adsorption volume of pores in the range 1.7–300 nm [cm^3/g]	0.462	0.452
BJH adsorption average pore diameter [nm]	12.00	36.43
DFT pore volume [cm^3/g]	0.00948 in pores ≤ 0.55 nm diameter	0.00000 in pores ≤ 1.05 nm diameter

As mentioned in the materials and methods, the BET surface area was calculated from a BET plot in the appropriate pressure range. A value of C gives information on the shape of adsorption isotherm in the BET range. There is general agreement that point B is well defined when the C value is higher than ~ 80 (Thommes et al., 2015). This allows to identify the stage of completion of the monolayer and the onset of multilayer adsorption. In addition, a high value of C for TDAC can be associated with filling of narrow micropores (Thommes et al., 2015).

Although the micropore surface areas calculated with the t-plot (Table 1) and DFT (Fig. 4) methods for TDAC and TPC show only qualitative agreement, the ratio of surface area development due to activation is almost the same regardless of the calculation method (5.4 for t-plot and 6.7 for DFT).

There is satisfactory agreement between the total pore volume (TPV) calculated with the Gurvich method (Table 1) and DFT model (Fig. 3). The relative errors are 13% and 15% for TDAC and TPC, respectively.

The average pore diameters calculated from the adsorption branch of nitrogen isotherms by BJH method show 12 nm and ~ 36 nm for TDAC and TPC, respectively.

Figure 5 presents an example SEM image and the corresponding binary representation obtained for the TDAC sample. This single SEM image contains 931 particles and 912 total cross-sectional areas. SA was made on the basis of all collected SEM micrographs after averaging the data. Table 2 compares the averaged results for TPC and TDAC.

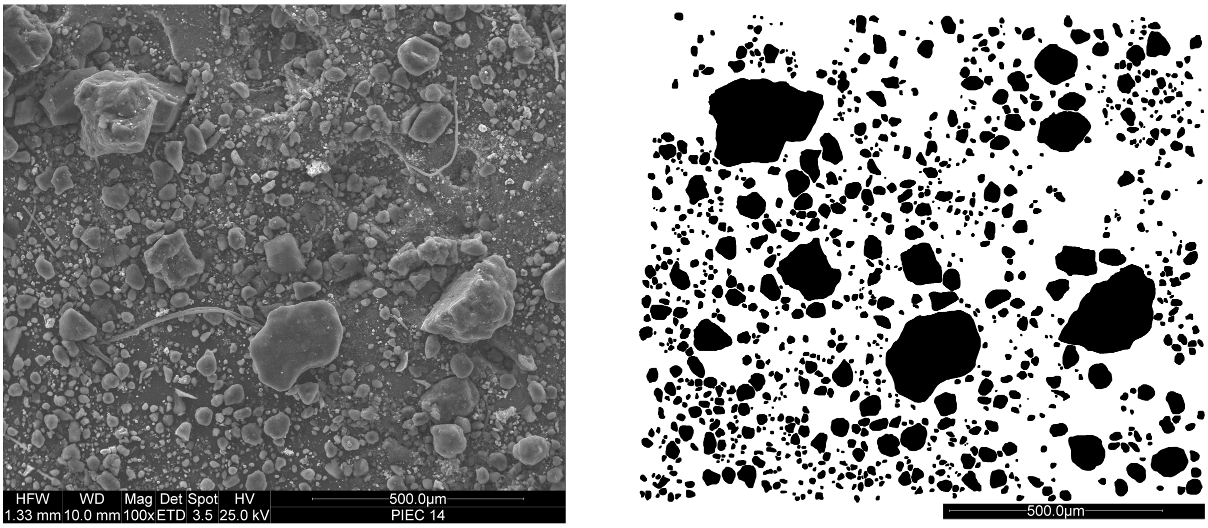

Fig. 5. SEM image of TDAC (in a mixed mode of BSE and SE) – left hand side, corresponding binarised image – right hand side

Table 2. Stereological characteristics of TPC and TDAC

TPC							
	A [μm^2]	d_2 [μm]	$d_{\min}$ [μm]	$d_{\max}$ [μm]	p [μm]	l_{rel}	p_{rel}
$\bar{X}$	378.0	16.4	14.4	20.0	58.5	1.40	1.13
σ^2	2589676.7	210.9	171.0	313.8	2834.3	0.0446	0.00275
σ	1609.2	14.5	13.0	17.7	53.2	0.248	0.052
CV	4.2	0.883	0.904	0.882	0.908	0.150	0.046
TDAC							
	A [μm^2]	d_2 [μm]	$d_{\min}$ [μm]	$d_{\max}$ [μm]	p [μm]	l_{rel}	p_{rel}
$\bar{X}$	477.7	18.4	16.2	22.6	66.1	1.41	1.13
σ^2	4033073	268.8	215.9	418.1	3772.0	0.055	0.00316
σ	2008.2	16.3	14.6	20.4	61.4	0.2	0.056
CV	4.20	0.889	0.904	0.902	0.929	0.166	0.049

The results show that the most common particle equivalent diameter, d_2, is in a range between 10 and 15 μm for both compared materials. In addition, a thorough analysis shows a very small difference between the frequencies of the most common particle equivalent diameter in this range (29.6% for TPC against 28.1% for TDAC). No significant difference has been found between the TPC and TDAC samples in terms of shape factors. The shape factors calculated from the $d_{\max}/d_2$ and p/d_2 ratios indicate that the grains of both samples are quasi-spherical and slightly elongated (Wejrzanowski and Kurzydlowski, 2003; Wejrzanowski et al., 2008). However, it is worth noting that there is a 25% increase in the mean particle cross-section surface area for the activated sample (TDAC).

Figure 6 shows the experimental adsorption isotherms for n-hexane at 298 K and 313 K. The repeatability of the results was checked by performing a series of measurements that showed remarkably close agreement (see an insert in Fig. 6). As a result, the individual isotherms were averaged. Given that VOC removal usually concerns diluted gas streams, the n-hexane adsorption isotherms were measured up to the relative pressure of $P/P^0 = 0.62$ (at $T = 298.15$ K) and $P/P^0 = 0.43$ (at $T = 313.15$ K).

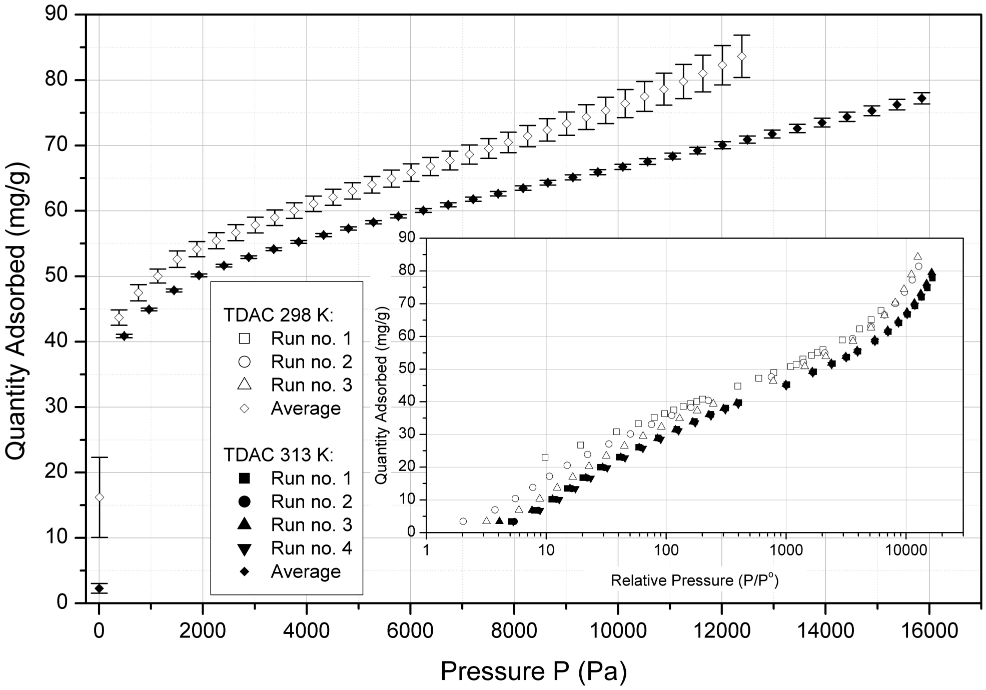

Fig. 6. The averaged experimental adsorption isotherm of n-hexane on TDAC at 298 K and 313 K (the error bars stand for the standard deviations). The insert shows the individual experimental adsorption isotherms

The micropore volume and characteristic adsorption energy (Table 3) were calculated from a characteristic curve, i.e. linearized Eq. (10) shown in Fig. 7. The affinity coefficient for n-hexane was calculated using the below correlation proposed by Wood (2001).

$$\beta = 0.00827X^{0.9} \tag{11}$$

where X is the n-hexane molecular parachor equal to 271.0 (Wood et al., 2001).

Table 3. Micropore volumes calculated with the N2-NLDFT and D-A models and characteristic adsorption energy obtained from the D-A isotherm model

Micropore volume, V_0^{DFT} [cm^3/g]	Micropore volume, $V_0^{\text{D-A}}$ [cm^3/g]	Characteristic adsorption energy, E_0 [kJ/mol]
0.0737	0.0750	14.87

The best agreement between the experimental isotherms at 298 and 313 K and the linearised Eq. (10) was found for the exponent of D–A isotherm $n = 2.992$.

Note that micropore volumes calculated with the N2-NLDFT (Fig. 3) and D–A (Fig. 6) models show very good agreement (Table 3).

Table 4 details parameters of seven selected adsorption isotherms and the associated error functions. Three (Langmuir and Freundlich), four (Sips, Toth and EL) and five (A–D–Toth and A–D–Sips) parameter

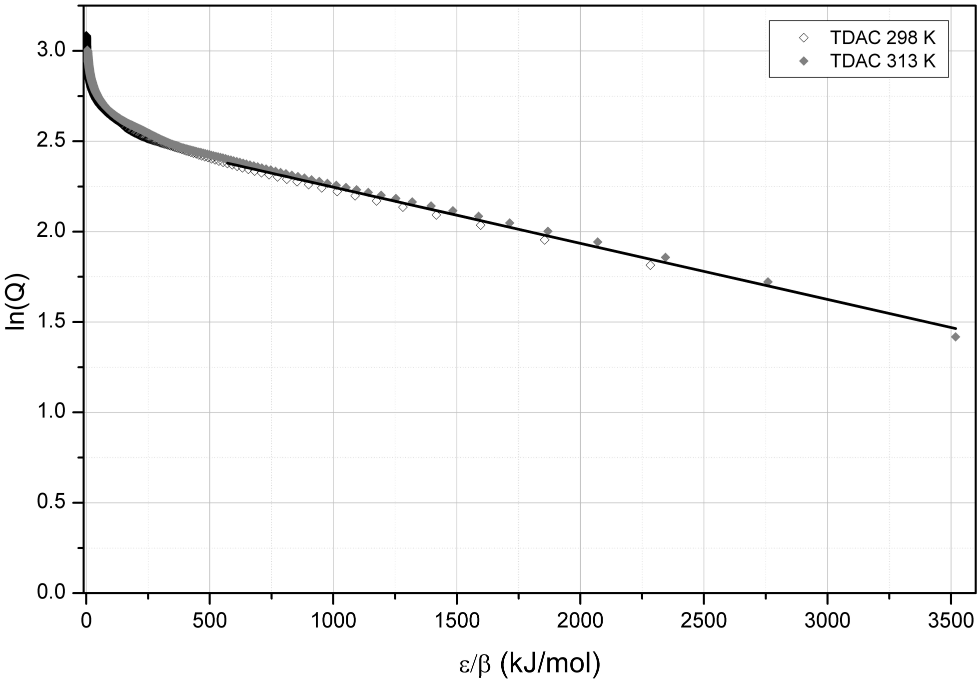

Fig. 7. Characteristic curve for TDAC

isotherms were employed to estimate the adsorption capacities of TDAC at different equilibrium pressures of *n*-hexane. The isotherm parameters were calculated using the following error functions (Foo and Hameed, 2010):

- Average Relative Error (ARE)

$$\mathrm{ARE} = \frac{100}{n}\sum_{i=1}^{n}\left|\frac{q_{e,cal}-q_{e,\exp}}{q_{e,\exp}}\right|_i \tag{12}$$

- Sum Square Error (SSE)

$$\mathrm{SSE} = \sum_{i=1}^{n}\left(q_{e,cal}-q_{e,\exp}\right)_i^2 \tag{13}$$

- Hybrid Fractional Error Function (HYBRID)

$$\mathrm{HYBRID} = \frac{100}{n-k}\sum_{i=1}^{n}\left(\frac{\left(q_{e,cal}-q_{e,\exp}\right)^2}{q_{e,\exp}}\right)_i \tag{14}$$

Table 4. Adsorption isotherm parameters calculated with different error functions. Bold parameters refer to the sets with the lowest sum of normalised error. ARE – Average Relative Error, SSE – Sum Square Error, HYBRID – Hybrid Fractional Error Function, SNE – Sum of Normalised Error

	ARE	SSE	HYBRID
Langmuir: $q_{\max}$	74.080	74.080	71.464
Langmuir: K_{L0}	7.069×10^{-8}	7.069×10^{-8}	1.701×10^{-6}
Langmuir: ΔH_{ads}	–25309.94	–25309.94	–17860.00

ARE	***7.924***	***7.924***	*8.101*
SSE	***67533.070***	***67533.070***	*73381.271*
HYBRID	*67.392*	*67.392*	***66.358***
SNE	*8.592*	*120.869*	***3.727***
Freundlich: K_{F0}	1.607	1.337	1.336
Freundlich: ΔH_{ads}	–5168.40	–5485.74	–5488.51
Freundlich: n	5.282	5.070	5.075
ARE	***2.733***	*2.867*	*2.845*
SSE	*8591.223*	***7301.589***	*7310.405*
HYBRID	*10.030*	*9.234*	***9.226***
SNE	*0.486*	*49.440*	***0.143***
Sips: $q_{\max}$	24358.544	22105.514	4799.783
Sips: K_{S0}	6.569×10^{-5}	5.994×10^{-5}	2.695×10^{-4}
Sips: ΔH_{ads}	–5177.96	–5504.78	–5558.14
Sips: n	5.272	5.057	5.020
ARE	***2.735***	*2.868*	*2.856*
SSE	*8618.355*	***7319.287***	*7393.515*
HYBRID	*10.044*	***9.241***	*9.246*
SNE	*0.487*	*49.739*	***0.146***
Toth: $q_{\max}$	632.659	3371.964	21288.277
Toth: K_{T0}	0.0403	622.646	3.1346×10^{9}
Toth: ΔH_{ads}	–29483.22	–28938.71	–28387.80
Toth: n	0.0878	0.0541	0.0366
ARE	*3.103*	*3.091*	***2.981***
SSE	*11495.292*	*8950.023*	***8402.612***
HYBRID	*10.568*	*9.491*	***9.248***
SNE	*0.878*	*104.991*	***0.195***
EL: $q_{\max}$	53.101	53.566	53.106
EL: K_{EL0}	3.320×10^{-6}	3.173×10^{-6}	4.350×10^{-6}
EL: ΔH_{ads}	–19877.56	–20168.26	–19878.81
EL: n	0.782	0.780	0.782
ARE	***2.283***	*2.497*	*2.463*
SSE	*7142.045*	*6774.769*	***6742.093***
HYBRID	*7.672*	*7.127*	***6.573***

SNE	*3.140*	*37.372*	***0.956***
A–D–Toth: $q_{\max}$	111.539	163.237	81.024
A–D–Toth: K_{ADT0}	2.792×10^{-2}	1.151	2.261×10^{-4}
A–D–Toth: ΔH_{ads}	–16288.42	–17547.22	–18538.06
A–D–Toth: t	0.181	0.126	0.298
A–D–Toth: n	0.277	0.265	0.319
ARE	***1.266***	*1.343*	*1.496*
SSE	*1822.025*	***1541.201***	*2444.460*
HYBRID	*3.949*	*4.784*	***2.849***
SNE	*0.274*	*9.685*	***0.179***
A–D–Sips: $q_{\max}$	86.779	114.324	72.918
A–D–Sips: K_{ADS0}	1.550×10^{-6}	2.052×10^{-7}	2.821×10^{-6}
A–D–Sips: ΔH_{ads}	–17666.56	–17640.37	–18374.89
A–D–Sips: d	3.074	4.094	2.300
A–D–Sips: n	0.4030	0.5278	0.3962
ARE	***1.268***	*1.325*	*1.557*
SSE	*1880.187*	***1417.18***	*2604.138*
HYBRID	*4.246*	*5.764*	***3.377***
SNE	*0.260*	*6.862*	***0.145***

Given that minimising these error functions provides different sets of isotherm parameters, the best set of parameters was chosen using the criterion of sum of the normalized errors (SNEs) (Foo and Hameed, 2010; Porter et al., 1999). SNE results from dividing an error function by its maximum error.

As can be seen in Table 4, the lowest SNE values are always achieved by the HYBRID error function, which indicates the most optimal sets of parameters for each of the isotherms.

Clearly, the Langmuir isotherm provides the worst fit to the experimental data. This is not particularly surprising given the fact that the Langmuir isotherm is restricted to the monolayer adsorption, which is typical for chemisorption and not physisorption. It is worth noting that despite the fact that the Langmuir isotherm gives the worst fit, its parameters are very often reported in the literature, which allows comparison and discussion of results in different articles.

The other adsorption isotherms are much better alternatives and the differences between them are very small (Fig. 8). However, a comparison of SNE values listed in Table 4 indicates the following order of fitting quality: Freundlich > A–D–Sips > Sips > A–D–Toth > Toth > EL > Langmuir.

As far as we know, the n-hexane adsorption on TDAC has not been previously reported in the literature. However, our results can be discussed with the n-hexane adsorption on other carbonaceous adsorbents. Interestingly, there is a large discrepancy in the reported data for activated carbons. In Hernández-Monje et al. (2018), adsorption of n-hexane at 263 K was investigated on five activated carbons with different surface physicochemical properties. The highest n-hexane adsorption of 0.27 mmol/g (23.27 mg/g) was

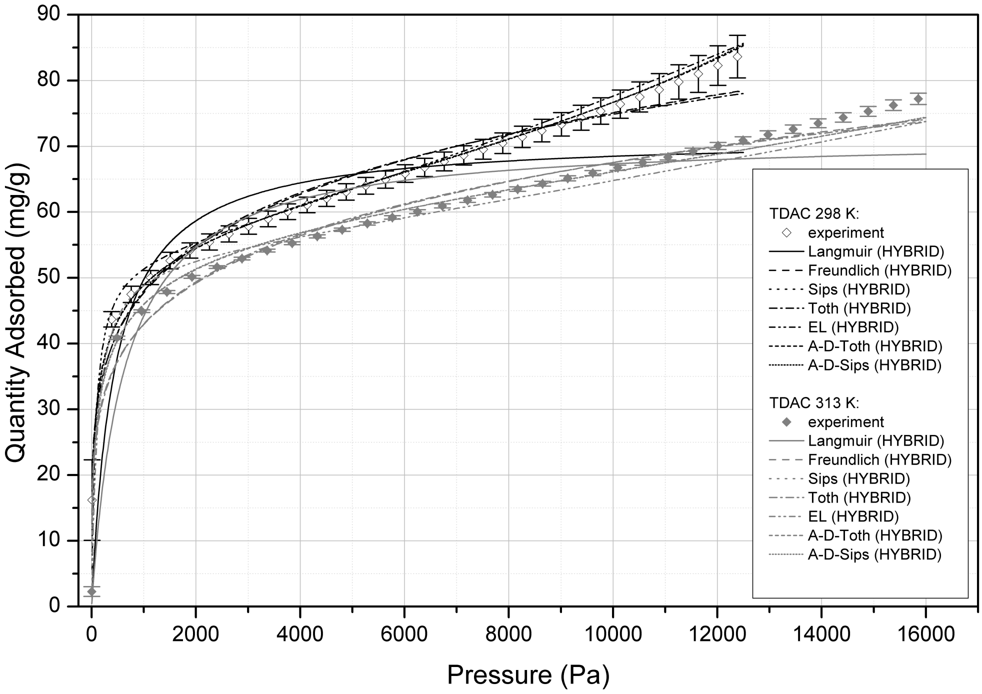

Fig. 8. Comparison of adsorption equilibrium isotherms

reported for the activated carbon with the lowest content of oxygenated groups (0.30 µmol/g) and the highest surface area (996 m^2/g). On the other hand, this sample displayed a fivefold increase compared to the *n*-hexane adsorption on the virgin activated carbon (4.48 mg/g). The *n*-hexane adsorption capacity of about 1.9 mmol/g (164 mg/g) at 1000 Pa can be read from the adsorption isotherm at 288 K presented in (Do and Do, 2002). In (Lai et al., 2009), the maximum monolayer coverage capacity according to the Langmuir model, $q_{\max}$, was 237.53 mg/g at 298 K for the *n*-hexane adsorption on a commercial activated carbon. Similar values of $q_{\max}$ were found by Kim et al. (2001), where two commercial activated carbons (X-7000 and SLG-2PS) were utilised for adsorption of *n*-hexane, giving 2.47 mol/kg (212.86 mg/g) for X-7000 and 3.15 mol/kg (271.47 mg/g) for SLG-2PS at 308.15 K. Surprisingly, another value of $q_{\max}$ = 3.625 mol/kg (312.40 mg/g) was reported for the same SLG-2PS commercial activated carbon in another work (Shim et al., 2003). Apart from different activated carbons, *n*-hexane adsorption was studied on activated carbon fabric (ACF) cloth (Singh et al., 2002) and the carbon aerogel and xerogel (Vivo-Vilches et al., 2018). For ACF cloth, a value of $q_{\max}$ = 188.67 mg/g at 303.15 K was determined. For the AC16 carbon aerogel and three carbon xerogels differing in the sample burn-off after activation (AC16X, AC16X10, AC16X40), the reported $q_{\max}$ values were: 1.45 mol/kg (124.96 mg/g), 1.06 mol/kg (91.35 mg/g), 2.02 mol/kg (174.08 mg/g) and 2.45 mol/kg (211.14 mg/g), respectively. Not surprisingly, the adsorptive performance of commercial activated carbons was better than that of TDAC sample. However, some results mentioned above display similar or even worse adsorption capacity for *n*-hexane than the TDAC sample. In summary, the adsorption capacity of TDAC is about 16.2 times higher for the TDAC sample than that of the worst reference material (Hernández-Monje et al., 2018), and 4.3 times lower than the best reference material (Shim et al., 2003).

4. SUMMARY AND CONCLUSIONS

Pyrolysis has recently become a more and more commonly used method of recycling ELTs. To improve its economics, much research effort has been devoted to valorisation of TPC by its activation. Until now, TDAC has proved to be a good candidate for water purification from various pollutants. On the other hand, the literature on the use of TDAC for gas phase adsorption is poor. This work investigates a potential application of TDAC for *n*-hexane adsorption from the gas phase. *n*-hexane is chosen as a representative of the wide class of VOCs.

The CO_2-activated TPC has better textural properties compared to its non-activated counterpart showing the BET and micropore surface areas of 259 and 70 m^2/g, respectively. Micropore volume and micropore surface area are 5.8 and 6.7 times higher for TDAC than TPC at $\sim$ 2 nm, respectively. Moreover, SA revealed that the grains of TPC and TDAC are quasi-spherical and slightly elongated with a 25% increase in the mean particle cross-section surface area for the activated sample (TDAC).

The isotherm parameters providing close fit to the experimental data were calculated using three different error functions: ARE, SSQ and Hybrid. A comparison of the normalised errors showed that the best fit was obtained with the Freundlich isotherm.

Importantly, we believe that our findings fill the knowledge gap regarding VOC adsorption on TDAC. However, other complementary studies are still needed to address the question on the possible practical use of TDAC. It seems necessary to study the problem from an economic perspective and compare the costs of TDAC production with the prices of activated carbons. On the other hand, the problem should be assessed from a circular economy perspective since valorisation of TPC by its activation improves economics of ELT pyrolysis as a whole, contributing to improving environmental protection.

We thank Prof. Tomasz Wejrzanowski for his valuable discussions and providing a free access to the MicroMeter software.

SYMBOLS

A	real surface area of cross-section of particle, μm^2
CV	$= \dfrac{\sqrt{V(X)}}{\bar{X}}$ standard deviation of variable x_i
d_2	$= (4 \cdot A/\pi)^{0.5}$ equivalent diameter, i.e. the diameter of a circle with the same surface area (A) as a given grain, μm
d	Aranovich–Donohue–Sips (A–D–Sips) constant, –
$d_{\min}$	grain shortest chord, μm
$d_{\max}$	grain longest chord, μm
E_0	characteristic adsorption energy (for standard vapour), J/mol
ΔH_{ads}	molar adsorption enthalpy, J/mol
K_{ADS}	Aranovich–Donohue–Sips (A–D–Sips) isotherm constant, Pa^{-1}
K_{ADT}	Aranovich–Donohue–Toth (A–D–Toth) isotherm constant, Pa^{-1}
K_{EL}	Extended Langmuir (EL) isotherm constant, Pa^{-1}
K_F	Freundlich isotherm constant, mg/g $\text{Pa}^{-1/n}$
K_i	equilibrium adsorption constant, the unit depends on used model (the same as the unit of used model)
K_{i0}	pre-exponential coefficient from equation describing the equilibrium adsorption constant, the unit is the same as K_i
K_L	Langmuir constant, Pa^{-1}
K_S	Sips constant, $\text{Pa}^{-1/n}$
K_T	Toth isotherm model constant, Pa^{-1}
k	number of adsorption isotherm parameters, –
l_{rel}	$= d_{\max}/d_{\min}$ the relative grain elongation, –

n	Freundlich, Sips, Tooth, Dubinin–Radushkevich (D–R), Extended Langmuir (EL), Aranovich–Donohue (A–D), Aranovich–Donohue–Tooth (A–D–Tooth) or Aranovich–Donohue–Sips (A–D–Sips) isotherm constant (exponent of equilibrium pressure), –
P	system pressure, Pa
p	perimeter of particle determined on the basis of the sum of the lengths of the mapping curve with the ends located at nodal points, µm
P^0	saturated vapour pressure, Pa
P/P^0	relative pressure, –
p_e	equilibrium pressure, Pa
p_{rel}	$= p/(\pi \cdot d_2)$ the relative grain perimeter, –
R	universal gas constant, J/(mol·K)
Q_0	maximum volume of adsorbate per adsorbed mass, the micropore volume, cm^3/g
Q_e	volume of adsorbate filling the micropores, in the unit mass of adsorbent, cm^3/g
q_e	equilibrium adsorption capacity, mg/g
$q_{e,cal}$	calculated equilibrium adsorption capacity, mg/g
$q_{e,\exp}$	experimental equilibrium adsorption capacity, mg/g
q_m	maximum adsorption capacity in the Sips or Toth models, mg/g
$q_{\max}$	maximum adsorption capacity, mg/g
T	system's temperature, K
t	Aranovich–Donohue–Toth (A–D–Toth) constant, –
$V(X)$	$= \sigma^2 = \frac{1}{n}\sum\limits_{i=1}^{n}\left(x_i - \bar{X}\right)^2$ variance of variable x_i
X	n-hexane molecular parachor, kg$^{1/4}$·s$^{-1/2}$·m^3·mol^{-1}
$\bar{X}$	$= \frac{1}{n}\sum\limits_{i=1}^{n} x_i$ mean value of variable x_i

Greek symbols

β	affinity coefficient, –
ε	adsorption potential, J/mol
σ	$= \sqrt{V(X)}$ standard deviation of variable x_i

REFERENCES

Abbasi S., Foroutan R., Esmaeili H., Esmaeilzadeh F., 2019. Preparation of activated carbon from worn tires for removal of Cu(II), Ni(II) and Co(II) ions from synthetic wastewater. *Desalin. Water Treat.*, 141, 269–278. DOI: 10.5004/dwt.2019.23569.

Acevedo B., Barriocanal C., Lupul I., Gryglewicz G., 2015. Properties and performance of mesoporous activated carbons from scrap tyres, bituminous wastes and coal. *Fuel*, 151, 83–90. DOI: 10.1016/j.fuel.2015.01.010.

Acosta R., Nabarlatz D., Sánchez-Sánchez A., Jagiello J., Gadonneix P., Celzard A., Fierro V., 2018. Adsorption of bisphenol A on KOH-activated tyre pyrolysis char. *J. Environ. Chem. Eng.*, 6, 823–833. DOI: 10.1016/j.jece.2018.01.002.

Allen J.L., Gatz J.L., Eklund P.C., 1999. Applications for activated carbons from used tires: Butane working capacity. *Carbon*, 37, 1485–1489. DOI: 10.1016/S0008-6223(99)00011-1.

Antoniou N., Stavropoulos G., Zabaniotou, 2014. Activation of end of life tyres pyrolytic char for enhancing viability of pyrolysis – Critical review, analysis and recommendations for a hybrid dual system. *Renew. Sustain. Energy Rev.*, 39, 1053–1073. DOI: 10.1016/j.rser.2014.07.143.

Aranda A., Navarro M.V., García T., Murillo R., Mastral A.M., 2007. Temperature swing adsorption of polycyclic aromatic hydrocarbons on activated carbons. *Ind. Eng. Chem. Res.*, 46, 8193–8198. DOI: 10.1021/ie070849p.

Aranovich G.L., Donohue M.D., 1995. A new approach to analysis of multilayer adsorption. *J. Colloid Interface Sci.*, 173, 515–520. DOI: 10.1006/jcis.1995.1353.

Charpenteau C., Seneviratne R., George A., Millan M., Dugwell D.R., Kandiyoti R., 2007. Screening of Low cost sorbents for arsenic and mercury capture in gasification systems. *Energy Fuels*, 21, 2746–2750. DOI: 10.1021/ef070026c.

Council Directive 1999/31/EC of 26 April 1999 on the landfill of waste. *Off. J. Eur. Communities* L 182, 0001–0019.

Council Directive 91/156/EEC of 18 March 1991 amending Directive 75/442/EEC on waste. Off. *J. Eur. Communities* L 078, 32–37.

Cuadrado-Collados C., Rojas-Mayorga C.K., Saavedra B., Martinez-Escandell M., Osiński J.M., Moghadam P.Z., Fairen-Jimenez D., Silvestre-Albero J., 2019. Reverse hierarchy of alkane adsorption in Metal-Organic Frameworks (MOFs) revealed by immersion calorimetry. *J. Phys. Chem. C*, 123, 11699–11706. DOI: 10.1021/acs.jpcc.9b01381.

Daraei H., Mittal A., 2017. Investigation of adsorption performance of activated carbon prepared from waste tire for the removal of methylene blue dye from wastewater. *Desalin. Water Treat.*, 90, 294–298. DOI: 10.5004/dwt.2017.21344.

Directive 2004/42/CE of the European Parliament and of the Council of 21 April 2004 on the limitation of emissions of volatile organic compounds due to the use of organic solvents in certain paints and varnishes and vehicle refinishing products and amending Directive 1999/13/EC. *Off. J. Eur. Union* L 143, 87–96.

Directive 2010/75/EU of the European Parliament and of the Council of 24 November 2010 on industrial emissions (integrated pollution prevention and control). *Off. J. Eur. Union* L 334, 17–119.

Do D.D., Do H.D., 2002. Characterization of micro-mesoporous carbonaceous materials. Calculations of Adsorption isotherm of hydrocarbons. *Langmuir*, 18, 93–99. DOI: 10.1021/la010232r.

Dubinin, M.M., Radushkevich, L.V., Zaverina, E.D., 1947. Sorption and structure of active carbons. *Zhurnal Fizicheskoi Khimii*, 21, 1351–1362.

E.P.A. Clean Air Technology, 1999. Choosing an adsorption system for VOC: carbon, zeolite or polymers? *CATC Tech. Bull.*, EPA-456/F-99-004.

ETRMA, 2017. ELT Management figures 2014. Available at: https://www.etrma.org/library/elt-management-figures-2014/

ETRMA, 2018. ELT Management figures 2016. Available at: https://www.etrma.org/library/elt-management-figures-2016/

Foo K.Y., Hameed B.H., 2010. Insights into the modeling of adsorption isotherm systems. *Chem. Eng. J.*, 156, 2–10. DOI: 10.1016/j.cej.2009.09.013.

Freundlich H., 1907. Über die Adsorption in Lösungen. *Zeitschrift für Phys. Chemie*, 57U, 385–470. DOI: 10.1515/zpch-1907-5723.

Gregorová E., Uhlířová T., Pabst W., Diblíková P., Sedlářová I., 2018. Microstructure characterization of mullite foam by image analysis, mercury porosimetry and X-ray computed microtomography. *Ceram. Int.*, 44, 12315–12328. DOI: 10.1016/j.ceramint.2018.04.019.

Hajizadeh Y., Onwudili. J.A., Williams P.T., 2011. Removal potential of toxic 2378-substituted PCDD/F from incinerator flue gases by waste-derived activated carbons. *Waste Manag.*, 31, 1194–1201. DOI: 10.1016/j.wasman.2011.01.011.

Helleur R., Popovic N., Ikura M., Stanciulescu M., Liu D., 2001. Characterization and potential applications of pyrolytic char from ablative pyrolysis of used tires. *J. Anal. Appl. Pyrolysis*, 58–59, 813–824. DOI: 10.1016/S0165-2370(00)00207-2.

Hernández-Monje D., Giraldo L., Moreno-Piraján J., 2018. Study of hexane adsorption on activated carbons with differences in their surface chemistry. *Molecules*, 23, 476. DOI: 10.3390/molecules23020476.

Hofman M., Pietrzak R., 2011. Adsorbents obtained from waste tires for NO2 removal under dry conditions at room temperature. *Chem. Eng. J.*, 170, 202–208. DOI: 10.1016/j.cej.2011.03.054.

Kaminsky W., Mennerich C., 2001. Pyrolysis of synthetic tire rubber in a fluidised-bed reactor to yield 1,3-butadiene, styrene and carbon black. *J. Anal. Appl. Pyrolysis*, 58–59, 803–811. DOI: 10.1016/S0165-2370(00)00129-7.

Kim D.J., Shim W.G., Moon H., 2001. Adsorption equilibrium of solvent vapours on activated carbons. *Korean J. Chem. Eng.*, 18, 518–524. DOI: 10.1007/BF02698300.

Kosuge K., Kubo S., Kikukawa N., Takemori M., 2007. Effect of pore structure in mesoporous silicas on VOC dynamic adsorption/desorption performance. *Langmuir*, 23, 3095–3102. DOI: 10.1021/la062616t.

Kotkowski T., Cherbański R., Molga E., 2018. Acetone adsorption on CO_2-activated tyre pyrolysis char – Thermogravimetric analysis. *Chem. Process Eng.*, 39, 233–246. DOI: 10.24425/122946.

Lai M.-H., Chu R.Q., Huang H.-C., Shu S.-H., Chung T.-W., 2009. Equilibrium isotherms of volatile alkanes, alkenes, and ketones on activated carbon. *J. Chem. Eng. Data*, 54, 2208–2215. DOI: 10.1021/je800826d.

Langmuir I., 1917. The constitution and fundamental properties of solids and liquids. II. Liquids. *J. Am. Chem. Soc.*, 39, 1848–1906. DOI: 10.1021/ja02254a006.

Langmuir I., 1918. The adsorption of gases on plane surfaces of glass, mica and platinum. *J. Am. Chem. Soc.*, 40, 1361–1403. DOI: 10.1021/ja02242a004.

Lehmann C.M.B., Rostam-Abadi M., Rood M.J., Sun J., 1998. Reprocessing and reuse of waste tire rubber to solve air-quality related problems. *Energy Fuels*, 12, 1095–1099. DOI: 10.1021/ef9801120.

Li S.-Q., Yao Q., Chi Y., Yan J.-H., Cen K.-F., 2004. Pilot-scale pyrolysis of scrap tires in a continuous rotary kiln reactor. *Ind. Eng. Chem. Res.*, 43, 5133–5145. DOI: 10.1021/ie030115m.

Li S.-Q.Q., Yao Q., Wen S.-E.E., Chi Y., Yan J.-H.H., 2005. Properties of pyrolytic chars and activated carbons derived from pilot-scale pyrolysis of used tires. *J. Air Waste Manage. Assoc.*, 55, 1315–1326. DOI: 10.1080/10473289.2005.10464728.

Lian F., Huang F., Chen W., Xing B., Zhu L., 2011. Sorption of apolar and polar organic contaminants by waste tire rubber and its chars in single- and bi-solute systems. *Environ. Pollut.*, 159, 850–857. DOI: 10.1016/j.envpol.2011.01.002.

Lin H.-Y., Yuan C.-S., Chen W.-C., Hung C.-H., 2006. Determination of the adsorption isotherm of vapor-phase mercury chloride on powdered activated carbon using thermogravimetric analysis. *J. Air Waste Manage. Assoc.*, 56, 1550–1557. DOI: 10.1080/10473289.2006.10464561.

Makrigianni V., Giannakas A., Bairamis F., Papadaki M., Konstaninou I., 2017. Adsorption of Cr(VI) from aqueous solutions by HNO3-purified and chemically activated pyrolytic tire char. *J. Dispers. Sci. Technol.*, 38, 992–1002. DOI: 10.1080/01932691.2016.1216862.

Manirajah K., Sukumaran S.V., Abdullah N., Razak H.A., Ainirazali N., 2019. Evaluation of low cost-activated carbon produced from waste tyres pyrolysis for removal of 2-chlorophenol. *Bull. Chem. React. Eng. Catal.*, 14, 443–449. DOI: 10.9767/bcrec.14.2.3617.443-449.

Micromeritics Instrument Corporation 2013–2014, 2014. 3FLEX Surface Characterization Analyzer – Operator Manual.

Mui E.L.K., Ko D.C.K., McKay G., 2004. Production of active carbons from waste tyres – A review. *Carbon*, 42, 2789–2805. DOI: 10.1016/j.carbon.2004.06.023.

Murillo R., Navarro M.V., García T., López J.M., Callén M.S., Aylón E., Mastral A.M., 2005. Production and application of activated carbons made from waste tire. *Ind. Eng. Chem. Res.*, 44, 7228–7233. DOI: 10.1021/ie050506w.

Porter J.F., McKay G., Choy K.H., 1999. The prediction of sorption from a binary mixture of acidic dyes using single- and mixed-isotherm variants of the ideal adsorbed solute theory. *Chem. Eng. Sci.*, 54, 5863–5885. DOI: 10.1016/S0009-2509(99)00178-5.

Rouquerol J., Llewellyn P., Rouquerol F., 2007. Is the bet equation applicable to microporous adsorbents? *Stud. Surf. Sci. Catal.*, 160, 49–56. DOI: 10.1016/S0167-2991(07)80008-5.

Rouquerol J., Rouquerol F., Sing K.S.W., 1998. *Absorption by powders and porous solids*. Academic Press.

Saleh T.A., Gupta V.K., Al-Saadi A.A., 2013. Adsorption of lead ions from aqueous solution using porous carbon derived from rubber tires: Experimental and computational study. *J. Colloid Interface Sci.*, 396, 264–269. DOI: 10.1016/j.jcis.2013.01.037.

San Miguel G., Fowler G.D., Sollars C.J., 2002. Adsorption of organic compounds from solution by activated carbons produced from waste tyre rubber. *Sep. Sci. Technol.*, 37, 663–676. DOI: 10.1081/SS-120001453.

San Miguel G., Fowler G.D., Sollars C.J., 2003. A study of the characteristics of activated carbons produced by steam and carbon dioxide activation of waste tyre rubber. *Carbon*, 41, 1009–1016. DOI: 10.1016/S0008-6223(02)00449-9.

Shaid M.S.H.M., Zaini M.A.A., Nasri N.S., 2019. Isotherm, kinetics and thermodynamics of methylene blue dye adsorption onto CO2-activated pyrolysis tyre powder. *Desalin. Water Treat.*, 143, 323–332. DOI: 10.5004/dwt.2019.23565.

Sharma V.K., Mincarini M., Fortuna F., Cognini F., Cornacchia G., 1998. Disposal of waste tyres for energy recovery and safe environment – Review. *Energy Convers. Manag.*, 39, 511–528. DOI: 10.1016/S0196-8904(97)00044-7.

Shim W.G., Lee J.W., Moon H., 2003. Equilibrium and Fixed-bed adsorption of n-hexane on activated carbon. *Sep. Sci. Technol.*, 38, 3905–3926. DOI: 10.1081/SS-120024711.

Sing K.S.W., Everet D.H., Haul R.A.W., Moscou L., Pierotti R.A., Rouquerol J., Siemieniewska T., 1985. Reporting physisorption data for gas/solid systems with special reference to the determination of surface area and porosity. *Pure Appl. Chem.*, 57, 603–619. DOI: 10.1351/pac198557040603.

Singh K.P., Mohan D., Tandon G.S., Gupta G.S.D., 2002. Vapor-phase adsorption of hexane and benzene on activated carbon fabric cloth: Equilibria and rate studies. *Ind. Eng. Chem. Res.*, 41, 2480–2486. DOI: 10.1021/ie0105674.

Sips R., 1948. On the Structure of a catalyst surface. *J. Chem. Phys.*, 16, 490–495. DOI: 10.1063/1.1746922.

Smith Y.R., Bhattacharyya D., Willhard T., Misra M., 2016. Adsorption of aqueous rare earth elements using carbon black derived from recycled tires. *Chem. Eng. J.*, 296, 102–111. DOI: 10.1016/j.cej.2016.03.082.

Song M., Tang M., Lv S., Wang X., Jin B., Zhong Z., Huang Y., 2014. The pyrolysis of multi-component municipal solid waste in fixed bed reactor for activated carbon production. *J. Anal. Appl. Pyrolysis*, 109, 278–282. DOI: 10.1016/j.jaap.2014.05.018.

Tarazona P., 1985a. Erratum: Free-energy density functional for hard spheres. *Phys. Rev.*, A 32, 3148–3148. DOI: 10.1103/PhysRevA.32.3148.

Tarazona P., 1985b. Free-energy density functional for hard spheres. *Phys. Rev.*, A 31, 2672–2679. DOI: 10.1103/PhysRevA.31.2672.

Tarazona P., Marconi U.M.B., Evans R., 1987. Phase equilibria of fluid interfaces and confined fluids. *Mol. Phys.*, 60, 573–595. DOI: 10.1080/00268978700100381.

Thommes M., Kaneko K., Neimark A.V., Olivier J.P., Rodriguez-Reinoso F., Rouquerol J., Sing, K.S.W., 2015. Physisorption of gases, with special reference to the evaluation of surface area and pore size distribution (IUPAC Technical Report). *Pure Appl. Chem.*, 87, 1051–1069. DOI: 10.1515/pac-2014-1117.

Toth J., 1971. State equation of the solid-gas interface layers. *Acta Chem. Acad. Sci. Hung.*, 69, 311–328.

Uhlířová T., Hostaša J., Pabst W., 2014. Characterization of the microstructure of YAG ceramics via stereology-based image analysis. *Ceramics-Silikáty*, 58, 173–183.

Vivo-Vilches J.F., Pérez-Cadenas A.F., Maldonado-Hódar F.J., Carrasco-Marín F., Siquet C., Ribeiro A.M., Ferreira A.F.P., Rodrigues A.E., 2018. From carbon molecular sieves to VOCs filters: Carbon gels with tailored porosity for hexane isomers adsorption and separation. *Microporous Mesoporous Mater.*, 270, 161–167. DOI: 10.1016/j.micromeso.2018.05.010.

WBCSD, 2008. *Managing end-of-life tires. Full report*. World Business Council for Sustainable Development. Available at: https://www.wbcsd.org/Sector-Projects/Tire-Industry-Project/Resources/Managing-End-of-Life-Tires.

Wejrzanowski T., Kurzydlowski K.J., 2003. Stereology of grains in nano-crystals. *Solid State Phenom.* 94, 221–228. DOI: 10.4028/www.scientific.net/SSP.94.221.

Wejrzanowski T., Lewandowska M., Kurzydłowski K.J., 2010. Stereology of nano-materials. *Image Anal. Stereol.*, 29, 1–12. DOI: 10.5566/ias.v29.p1-12.

Wejrzanowski T., Spychalski W., Różniatowski K., Kurzydłowski K., 2008. Image Based Analysis of complex microstructures of engineering materials. *Int. J. Appl. Math. Comput. Sci.*, 18, 33–39. DOI: 10.2478/v10006-008-0003-1.

Williams P.T., 2013. Pyrolysis of waste tyres: a review. *Waste Manag.*, 33, 1714–28. DOI: 10.1016/j.wasman.2013.05.003.

Zhang P., Wang L., 2010. Extended Langmuir equation for correlating multilayer adsorption equilibrium data. *Sep. Purif. Technol.*, 70, 367–371. DOI: 10.1016/j.seppur.2009.10.007

Zhu Jianzhong, Liang H., Fang J., Zhu Jianguo, Shi B., 2011. Characterization of chlorinated tire-derived mesoporous activated carbon for adsorptive removal of toluene. *CLEAN – Soil, Air, Water*, 39, 557–565. DOI: 10.1002/clen.201000265.

Received 29 October 2019
Received in revised form 26 February 2020
Accepted 03 March 2020